

The distribution of stars around the Milky Way's central black hole: II. Diffuse light from sub-giants and dwarfs

R. Schödel¹, E. Gallego-Cano¹, H. Dong¹, F. Nogueras-Lara¹, A. T. Gallego-Calvente¹, P. Amaro-Seoane², and H. Baumgardt³

¹ Instituto de Astrofísica de Andalucía (CSIC), Glorieta de la Astronomía s/n, 18008 Granada, Spain e-mail: rainer@iaa.es

² Institut de Ciències de l'Espai (CSIC-IEEC) at Campus UAB, Carrer de Can Magrans s/n 08193 Barcelona, Spain
Institute of Applied Mathematics, Academy of Mathematics and Systems Science, Chinese Academy of Sciences, Beijing 100190, China

Kavli Institute for Astronomy and Astrophysics, Beijing 100871, China

Zentrum für Astronomie und Astrophysik, TU Berlin, Hardenbergstraße 36, 10623 Berlin, Germany

³ School of Mathematics and Physics, University of Queensland St. Lucia, QLD 4068, Australia

Received; accepted

ABSTRACT

Context. This is the second of three papers that search for the predicted stellar cusp around the Milky Way's central black hole, Sagittarius A*, with new data and methods.

Aims. We aim to infer the distribution of the faintest stellar population currently accessible through observations around Sagittarius A*.

Methods. We use adaptive optics assisted high angular resolution images obtained with the NACO instrument at the ESO VLT. Through optimised PSF fitting we remove the light from all detected stars above a given magnitude limit. Subsequently we analyse the remaining, diffuse light density. Systematic uncertainties are constrained by the use of data from different observing epochs and obtained with different filters. We show that it is necessary to correct for the line emission from ionised gas, which would otherwise lead to a systematically biased light density profile. We use a Paschen α map obtained with the Hubble Space Telescope for this purpose.

Results. The azimuthally averaged surface light density profile within a projected distance of $R \lesssim 0.5$ pc from Sagittarius A* can be described consistently by a single power law with an exponent of $\Gamma = 0.28 \pm 0.03$, similar to what has been found for the surface number density of faint stars in Paper I.

Conclusions. The analysed diffuse light arises from sub-giant and main-sequence stars with $K_s \approx 19 - 20$ with masses of $1 - 2 M_\odot$. These stars can be old enough to be dynamically relaxed. The observed power-law profile and its slope are consistent with the existence of a relaxed stellar cusp around the Milky Way's central black hole. We find that a Nuker law provides an adequate description of the nuclear cluster's intrinsic shape (assuming spherical symmetry). The 3D power-law slope near Sgr A* is $\gamma = 1.23 \pm 0.05$. The stellar density decreases more steeply beyond a break radius of about 3 pc, which corresponds roughly to the radius of influence of the massive black hole. At a distance of 0.01 pc from the black hole, we estimate a stellar mass density of $2.3 \pm 0.3 \times 10^7 M_\odot \text{pc}^{-3}$ and a total enclosed stellar mass of $180 \pm 20 M_\odot$. These estimates assume a constant mass-to-light ratio and do not take stellar remnants into account. The fact that no cusp is observed for bright ($K_s \lesssim 16$) giant stars at projected distances of roughly 0.1-0.3 pc implies that some mechanism has altered their appearance or distribution.

Key words. Galaxy: center – Galaxy: kinematics and dynamics – Galaxy: nucleus

1. Introduction

The existence of power-law stellar density cusps in dynamically relaxed clusters around massive black holes (BHs) is a fundamental prediction of theoretical stellar dynamics. The problem of a stationary stellar density profile around a massive, star-accreting BH was first analysed by Peebles (1972), followed by Frank & Rees (1976), Lightman & Shapiro (1977), and Bahcall & Wolf (1976). Eight years before Peebles (1972), Gurevich (1964) had obtained an analogous solution for the distribution of electrons in the vicinity of a positively charged Coulomb centre. Since then, many authors have worked on this problem with a broad variety of methods and have come to similar conclusions (see, e.g., Amaro-Seoane et al. 2004; Alexander 2005; Merritt 2006, and references therein).

The best-suited (and currently probably also only) environment where we can test the presence of such a cusp is the nuclear

star cluster around the massive black hole at the centre of the Milky Way (e.g., Genzel et al. 2010; Schödel et al. 2014b). Unfortunately, the observations have been limited to the red clump (RC) stars and brighter giants so far. The density profile of these stars appears to suggest the absence of a stellar cusp (Buchholz et al. 2009; Do et al. 2009; Bartko et al. 2010). However, these stars only represent a small fraction of the old stars in the nuclear cluster. It has been proposed that stellar collisions removed their envelopes in the innermost, densest regions of the cusp, which would render them invisible (see, e.g., Alexander 1999; Dale et al. 2009), but this cannot fully explain the observations. Another possibility, that has been recently put forward, is that they interacted in the past with (a) fragmenting gaseous disc(s), which is an efficient way to get rid of their envelopes (Amaro-Seoane & Chen 2014). The analytical solution of Amaro-Seoane & Chen (2014) was confirmed by Kieffer & Bogdanović (2016) with elaborate numerical simulations.

The fact that we are dealing with a fundamental problem of stellar dynamics, the ambiguity of the observational data and their interpretation, as well as the implications of stellar cusps for the frequency of Extreme-Mass Ratio Inspirals (EMRIs, see Amaro-Seoane et al. 2007 and the review Amaro-Seoane 2012 and references therein), and thus on the detection rate of sources of gravitational radiation (Hopman & Alexander 2005), have urged us to revisit this topic. In particular, the L3 mission of the European Space Agency has been approved to be devoted to low frequency gravitational wave astronomy, with EMRIs being an important class of potential sources. The mission implementing this science will follow the Laser Interferometer Space Antenna (LISA) mission concept (Amaro-Seoane et al. 2012, 2013) or a similar one, like the Chinese Taiji concept (Gong et al. 2015)..

This is the second one of a series of papers addressing the distribution of stars around Sagittarius A* (Sgr A*). They are closely related and use the same data, but focus on different methods and stellar populations. In this work we use the diffuse light density, while in our first paper (Gallego et al., from now on referred to as Paper I), we analyse the star counts from the brighter, resolved stellar population. We also refer the interested reader to the more detailed introduction of Paper I for more details about the history and the state-of-the-art of the investigation of the stellar cusp at the centre of the Milky Way.

Our primary goal is to find the predicted stellar cusp of the nuclear stellar cluster (NSC) around Sgr A*. To reach this aim, we push the boundaries of observational evidence by reaching toward fainter magnitudes and thus accessing a more representative sample of stars in the nuclear cluster. In Paper I, we show how we use stacking and improved analysis methods to provide acceptably complete star counts for stars about one magnitude fainter than what has been done up to now. These stars, of observed magnitudes $K_s \approx 18$ at the distance and extinction of the Galactic Centre (GC), are probably mostly sub-giant stars, with masses of $1 - 2 M_\odot$. They can therefore be old enough to be dynamically relaxed. Indeed, their distribution inside of a projected distance of $R \lesssim 0.5$ pc can be approximated well by a single power-law with a slope of $\Gamma \approx 0.36$. This finding is consistent with the existence of a stellar cusp of old stars around Sgr A*, as we discuss in Paper I. Here, we focus on the diffuse stellar light density around Sgr A*, which provides us with information on even fainter stars.

2. Data reduction and analysis

2.1. Basic reduction

We use the same H and K_s -band data obtained with the S27 camera of NACO/VLT that are used in Paper I and, additionally, K_s -band NACO/VLT S13 camera data from 4 May/12 June/13 August 2011, 4 May/9 August/12 September 2012, and 29 March/14 May 2013. We follow the same data reduction steps. The S13 images were stacked to provide a deep image, as done with the S27 images in paper I. In addition, we use the calibrated HST/NICMOS 3 image of the emission from ionised gas at $1.87 \mu\text{m}$, that was presented by Dong et al. (2011). Finally, we also make use of NACO/VLT S27 Brackett- γ (Br γ) narrow band (NB) observations, obtained on 5 August 2009, with a detector integration time (DIT) of 15 s, 3 averaged readouts per exposure ($NDIT = 3$), and 45 dither positions ($N = 45$). Data reduction was standard, as described in Paper I, including rebinning to a finer pixel scale by a factor of 2.

2.2. Source subtraction

Subtraction of detected stars is a critical step when estimating the diffuse light. A particular challenge in AO observations is the presence of the large seeing halo (FWHM on the order $1''$) around the near-diffraction limited core of the PSFs. The dynamic range of the detected stars comprises >10 magnitudes, from the brightest star, GCIRS 7 with $K_s \approx 7$ to the faintest detectable stars with $K_s \approx 19$ (see Paper I). Many of the brightest stars ($K_s = 9 - 11$) are young, massive stars concentrated in the IRS 16, IRS 1, IRS 33, or IRS 13 complexes in the central 0.5 pc (e.g., Genzel et al. 2003; Lu et al. 2005, 2009; Paumard et al. 2006). They must be carefully subtracted to avoid a bias in the surface light density. In addition, the PSF changes across the field due to anisoplanatic effects, and the variable source density and extinction mean that the faint wings of the PSFs cannot be estimated with similar signal-to-noise in all parts of the field because there is not a homogeneous density of bright, isolated stars.

As explained in Paper I, we extracted the PSFs on overlapping sub-fields, smaller than the isoplanatic angle. In each of these sub-fields we used about 10 isolated stars – the brightest ones possible – to estimate the PSF core. We then fitted the PSF halo determined from the brightest star in the field, GCIRS 7, to the cores. Schödel et al. (2010) have shown for NACO AO GC data that the variation of the PSF halo is rather negligible, which means that with the chosen approach we can reach a photometric accuracy of a few percent across the entire field. Subsequently, point sources are detected and subtracted. Since the detection of occasional spurious sources is no source of concern for this work, we chose a more aggressive approach than in Paper I, setting the *StarFinder* parameters $min_correlation = 0.70$ and $deblend = 1$ for all images (except if stated explicitly otherwise). We note that even with these settings the detection completeness falls below 50% for sources fainter than about $K_s = 18.0$ in the centralmost arcseconds.

In order to have an extinction map that covers even the large area of the wide field observations from May 2011, we created an extinction map from HAWK-I H and K_s speckle holography-reduced FASTPHOT observations of the central square arcminutes (Nogueras-Lara et al., in prep.). We used the extinction law of Schödel et al. (2010) ($A_\lambda \propto \lambda^{-2.2}$), assumed a constant intrinsic colour of $(H - K_s)_0 = 0.1$ for all the stars, and used the mean of the 20 nearest stars for each pixel. This results in an extinction map with a variable angular resolution of roughly $2''$. The results presented in this paper are not sensitive in any significant way on the variation in these assumptions within their uncertainties. In particular, changing the exponent of the extinction law to other plausible values (e.g., 2.0, see Nishiyama et al. 2009) will have an impact on any of the parameters of interest that is a factor of a few smaller than other sources of uncertainties that will be discussed here.

We demonstrate the result of this strategy in Fig. 1. There, we show the mosaic of the deep K_s image (see Paper I), and the same field after subtraction with a single, constant PSF, and after subtraction with a variable PSF, composed of a local core plus a global halo. As can be seen, using a single, constant PSF leads to variable artefacts associated with the stellar sources across the field (see also Schödel 2010). Also, when the wings of the PSF are not determined with high signal-to-noise, then the diffuse emission is dominated by flux from the seeing halos around bright stars.

With the variable core plus halo PSF (determined from the brightest star IRS 7, right panel), the residuals around bright stars

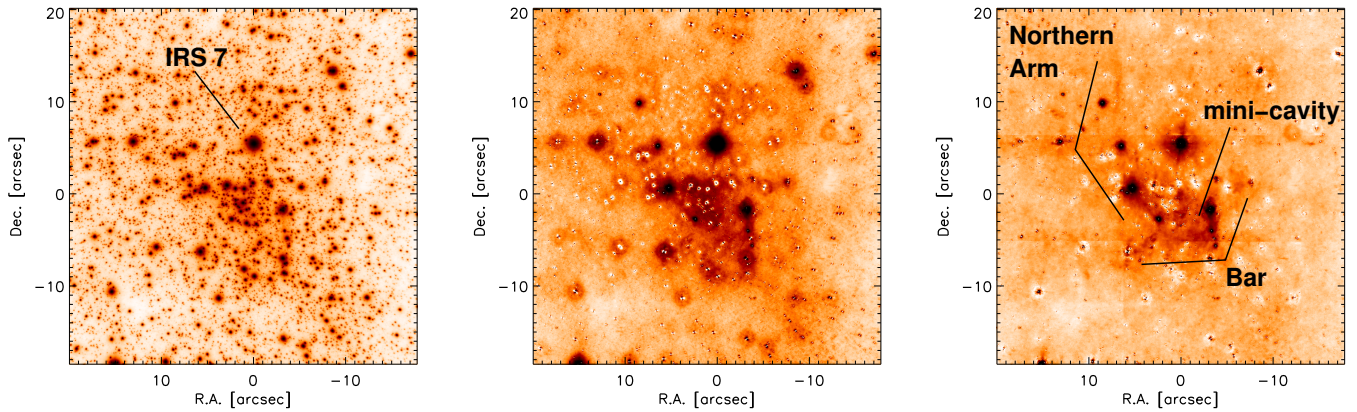


Fig. 1. Source subtraction. Left: Deep K_S -band mosaic (see Paper I). Middle: Deep K_S -band mosaic with all detected stars subtracted, using a single, constant PSF, for the entire field. Right: Deep K_S -band mosaic with all detected stars subtracted, using a locally extracted PSF kernel merged with a constant halo, that is estimated from IRS 7. Typical features of the mini-spiral of ionised gas are indicated. Logarithmic colour scale in all images, with the same scale used in the middle and right panels. North is up and east is to the left.

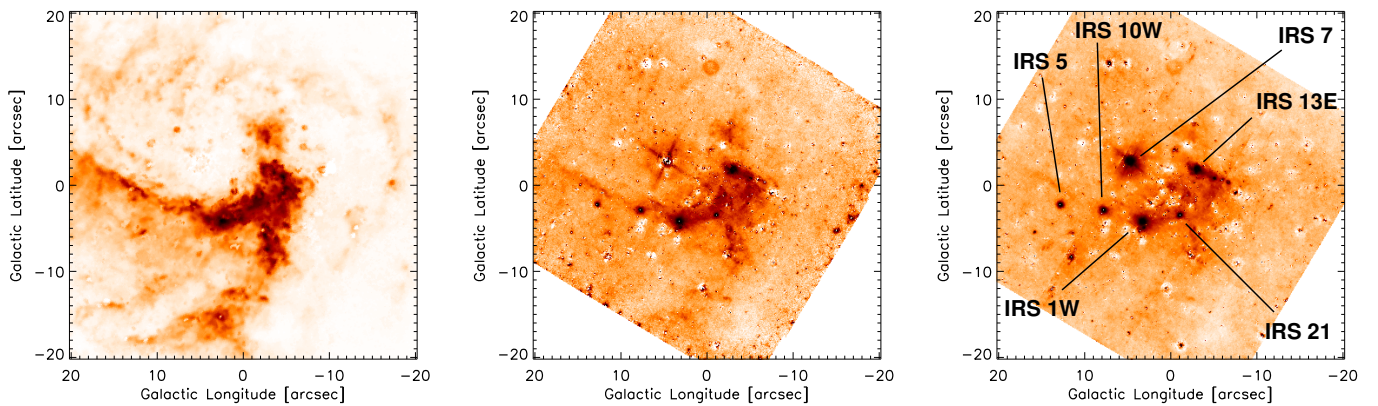


Fig. 2. Left: HST NIC3 point-source-subtracted Pa- α image of the GC. Middle: VLT NACO point-source-subtracted Br- γ image. Right: VLT NACO point-source-subtracted K_S continuum image. Some prominent non-line-emission sources (see text) are labeled.

are strongly suppressed and any remaining residuals are largely constant across the field, as can be seen in the right panel of Fig. 1. These remaining residuals are typical for PSF subtraction with an empirical PSF when the PSF is not fully constant across the field: Since several stars have to be used to derive a median PSF, their slightly different PSFs will result in a slightly too broad median PSF. This leads to the typical and inevitable artefacts in the form of core-excesses with surrounding negativities that can be seen around bright stars. Nevertheless, as can be seen, the residuals around the bright stars have been strongly suppressed with our method. The only exception is GCIRS 7, which is extremely bright (a few magnitudes brighter than any other source in the field). The filamentary structure of the ionised gas in the so-called mini-spiral (see Genzel et al. 2010, and references therein) becomes apparent, with features such as the northern arm, the bar, or the mini-cavity clearly visible.

2.3. Subtraction of ionised gas emission

As we can see in the right panels of Figs. 1 and 2, diffuse emission from ionised gas in the so-called mini-spiral (see., e.g., Genzel et al. 2010) contributes significantly to the diffuse emission

within about 0.5 pc ($\sim 12''$ for a GC distance of 8 kpc) of Sgr A*, even in broad band images. We therefore have to correct for it before we will be able to estimate the diffuse emission arising from unresolved *stellar* sources. At the wavelengths considered, the emission arises mostly from hydrogen and helium lines (e.g., H I at 2.17, 1.64 or 1.74 μm , He I at 1.70, 2.06, or 2.11 μm). In Fig. 2 we show the mini-spiral as seen in the Paschen α line with NIC3/HST and in the Brackett γ line as well as in K_S continuum with NACO/VLT, respectively. The Pa α image is from the survey by Wang et al. (2010) and Dong et al. (2011).

Since we will use the HST image as a reference for gas emission, we aligned all our images via a first order polynomial transform with the HST image. The positions of detected stars were used to calculate the transformation parameters with IDL POLY-WARP and the images were then aligned using IDL POLY_2D. The pixel scale of the resulting images is set to the one of the HST image (0.101'' per pixel).

As can be seen in Fig 2, the Pa α image traces the gas emission very clearly (with the exception of a few Pa α excess sources, see Dong et al. 2012) and the K_S and Br γ images of the diffuse emission trace the same structures of the mini-spiral. Some differences are given by residuals around bright

stars, by some residual emission associated with the brightest star, GCIRS 7, by hot dust emission around the probable bow-shock sources IRS 21, IRS 10W, IRS 5, and IRS 1W, and by enhanced emission in and around the IRS 13E complex, probably from a higher gas temperature. We mark some of these sources and areas in Fig. 2 and will mask them when deriving scaling factors for gas subtraction and when computing the brightness of diffuse stellar light in the following sections.

Figure 3 shows the point source-subtracted Br γ and K_S continuum images after subtraction of the scaled Pa α image. The scale factor was assumed constant and estimated by eye. All images were corrected for differential extinction. We also determined the scaling factor in a numerical way by producing an unweighted best χ^2 fit of the scaled Pa α image plus an azimuthally symmetric simple power-law diffuse light density centred on Sgr A* to the K_S image. The fitting region was limited to $R < 0.5$ pc within Sgr A* to avoid complications from a change of slope in the power-law at larger distances (see below). The resulting best-fit factor was identical - within the uncertainties - to our by-eye estimate. As can be seen in Fig. 3, most of the emission from the ionised gas in the mini-spiral can be effectively removed by this simple procedure. From our by-eye fit we estimated an uncertainty of 10% for the best scale factor. This uncertainty has a negligible effect on the parameters we are interested in, in particular the slope of the power-law surface density. For all images and wavelengths used in the following we applied the numerical procedure to estimate the scaling factor for the subtraction of the diffuse gas emission.

An alternative way of subtracting the ionised gas emission may be by using the intrinsic line ratio of Br γ /Pa α . However, this is not practical in our case because most of our data are broad-band observations and include additional lines, e.g. from the $2.058 \mu\text{m}$ He I line in the K_S -band. Also, in the case of the Br γ image, no accurate calibration was possible because no zero point observations were taken at the time of the observation and the sky conditions were not photometric.

3. The surface density of faint stars in the GC

In this section we explore the surface brightness (SFB) profile of the diffuse stellar light in observations taken with different cameras and filters, as well as at different epochs. We will also perform various checks on potential sources of systematic bias. In the following we will refer to a point-source subtracted image that has been corrected for extinction and for ionised gas emission as a *corrected image*.

3.1. Wide field K_S continuum

First, we examine a wide-field mosaic that was obtained with NACO/VLT S27 in May 2011. In total, 4×4 pointings were observed in K_S , centred approximately on Sgr A*. The images are relatively shallow, with a total on-target exposure time of only 72 s per pointing (4 exposures with $DIT = 2$ s, $NDIT = 9$), but of excellent and homogeneous quality.

Figure 4 shows the point-source subtracted wide-field image before and after correction for extinction and gas emission. As mentioned above, by assuming that the diffuse light from the stars follows a power law inside of $R = 0.5$ pc and that a constant scaling factor is adequate to remove the emission from the ionised gas, we can numerically fit both the power-law index and the scaling factor. We varied the fitting region and the potential additive offset of the diffuse emission (see below) and

found that they had a negligible influence on the best-fit factor. We then subtracted the extinction-corrected Pa α image from the extinction-corrected diffuse emission.

We measured the mean diffuse emission in annuli around Sgr A*, using the IDL ASTROLIB routine ROBUST_MEAN and rejecting $> 3\sigma$ outliers. The corresponding uncertainties were taken as the uncertainties of the means. The resulting SFB profiles, both raw and after subtraction of the scaled Pa- α emission, are shown in Fig. 5. The error bars are probably underestimated because there are systematic effects present in our corrected images that are very difficult to assess or correct quantitatively, e.g.: The assumption of a constant emission ratio of Paschen- α to line emission in K_S , uncertainties of the extinction map and assumed extinction law, or systematics related to the subtraction of very bright stars.

We fitted a simple broken power-law to the data:

$$\Sigma(R) = n_0 * (R/R_0)^{-\Gamma_{in,out}}, \quad (1)$$

where $\Sigma(R)$ is the surface flux density at a projected distance R , n_0 is the normalisation of the SFB, R_0 is the break radius, and $\Gamma_{in,out}$ are the power-law indices inside and outside of R_0 . Since we do not know the correct statistics of the error bars, we interpret the reduced χ^2_{red} values as orientative, to infer whether a fit is better or worse, and then rescale the errors of the best-fit parameters to a reduced $\chi^2 = 1$. In the following, we explore the influence of some of the possible systematic effects on the results.

First, we note that a simple power-law provides a clearly worse fit ($\chi^2_{red} \approx 26$) to the corrected data than a broken power-law fit ($\chi^2_{red} \approx 7$). Also, we note that the broken power-law fit to the uncorrected data, with a $\chi^2_{red} \approx 17$, is worse than the one for the corrected data, with a $\chi^2_{red} \approx 7$. The best fits were computed with the IDL MPFIT package (Markwardt 2009). We found that the formal uncertainties of the fits, as provided by MPFIT, were significantly smaller than the uncertainties due to systematics (see below), even after rescaling to $\chi^2_{red} = 1$. We found no significant differences between weighted and unweighted fits (in this case and all others in this work).

Our experiments with the data suggest that the strongest systematic effect can arise from an unknown additive offset of the diffuse emission. Although the images were sky-subtracted – the sky background in the corresponding filters was measured on a dark cloud at a few arcminutes offset – there is some uncertainty related to this procedure: There was only one sky measurement done for the approximately one hour-long observations. Hence, the sky background may have varied. Also, we are interested in the SFB profile of the nuclear star cluster, but there may be diffuse flux contributions from other structures, such as the nuclear stellar disk (see Launhardt et al. 2002). Fortunately, there are several dark clouds contained in the field-of-view (FOV). Those clouds belong most probably to dense gas and dust in the so-called circumnuclear ring (CNR) in front of the nuclear star cluster (see, e.g., Ekers et al. 1983; Lo & Claussen 1983; Christopher et al. 2005) and can thus serve to estimate the flux offset. We measured the median flux density on four positions within these dark clouds (see Fig. 3) and thus obtained an estimate for the mean and standard deviation of the constant diffuse flux offset. The surface flux density measurements were then repeated after subtracting the mean offset and the two values resulting from adding or subtracting its standard deviation. The extinction correction was performed after the subtraction of this potential background bias. We thus could estimate the uncertainty of the fit parameters. We obtained: $n_0 = 20.8 \pm 1.2$ mJy, $R_0 = 0.56 \pm 0.01$ pc, $\Gamma_{in} = 0.29 \pm 0.01$, and $\Gamma_{out} = 0.66 \pm 0.08$.

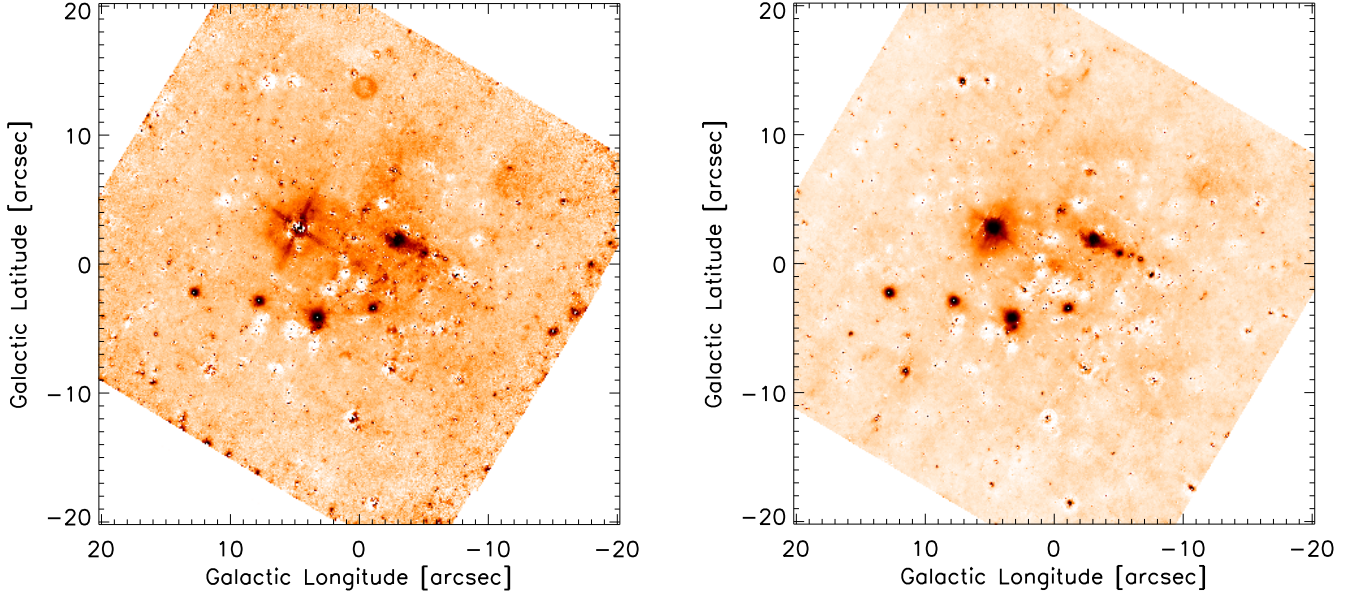


Fig. 3. Left: Point-source-subtracted Br- γ image minus scaled Pa- α image. Right: Point-source-subtracted K_S continuum image minus scaled Pa- α image.

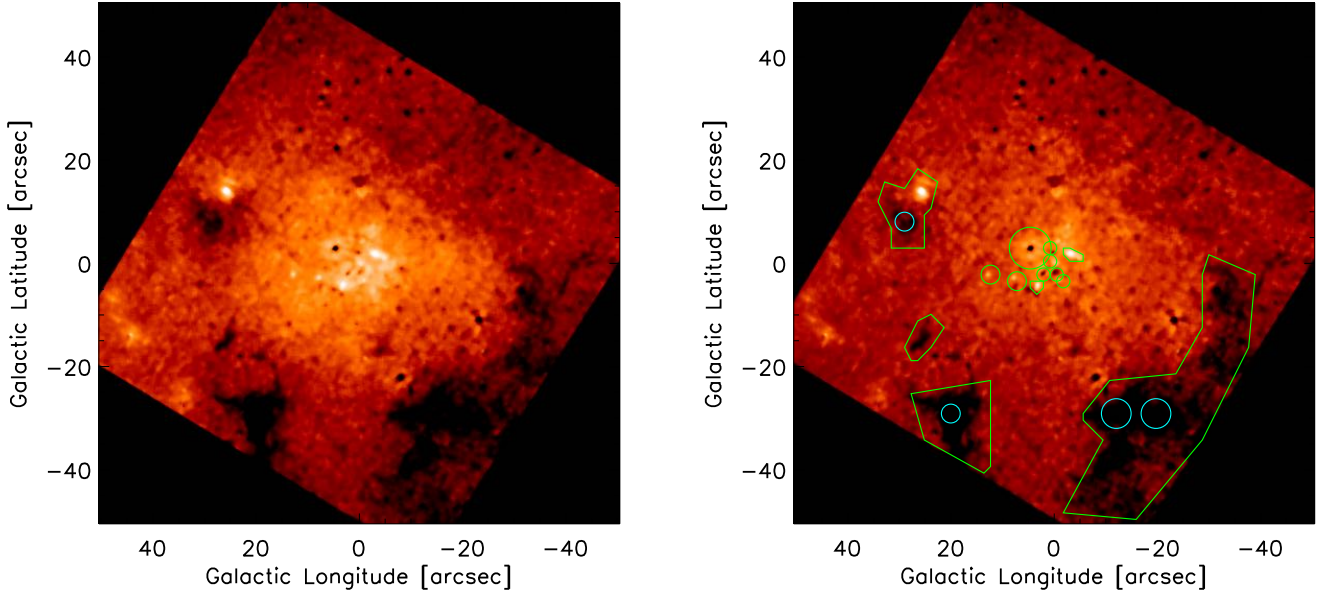


Fig. 4. Left: Point-source-subtracted K_S wide field continuum image. Right: Image corrected for extinction and ionized gas emission. Contaminated regions (residua from bright stars, hot dust, and IRS 13) and dark clouds, that are excluded from measuring the surface light density, are indicated by green polygons. The blue circles indicate regions that were used to estimate the offset of the diffuse flux density.

It is also important to assess the influence of the extinction correction on our results. We therefore repeated the procedure without correction for differential extinction, i.e. assuming a spatially constant extinction of $A_{K_S} = 3.0$, equivalent to the median over the field. The corresponding SFB profile is shown in the middle panel of Fig. 5. It is similar to the one with differential extinction correction, but there are some small differences, such as a flattening at the largest distances. The best-fit parameters

are somewhat different, but the power-law indices agree within their 1σ uncertainties: $n_0 = 26.7 \pm 2.1$ mJy, $R_0 = 0.44 \pm 0.03$ pc, $\Gamma_{in} = 0.29 \pm 0.03$, and $\Gamma_{out} = 0.76 \pm 0.08$.

When studying stellar number densities, as in Paper I, assessing and correcting incompleteness due to sensitivity and, in particular, crowding can have significant effects on the results. In our study of the diffuse light density, bias related to completeness could occur as well. The contribution of the occasional bright

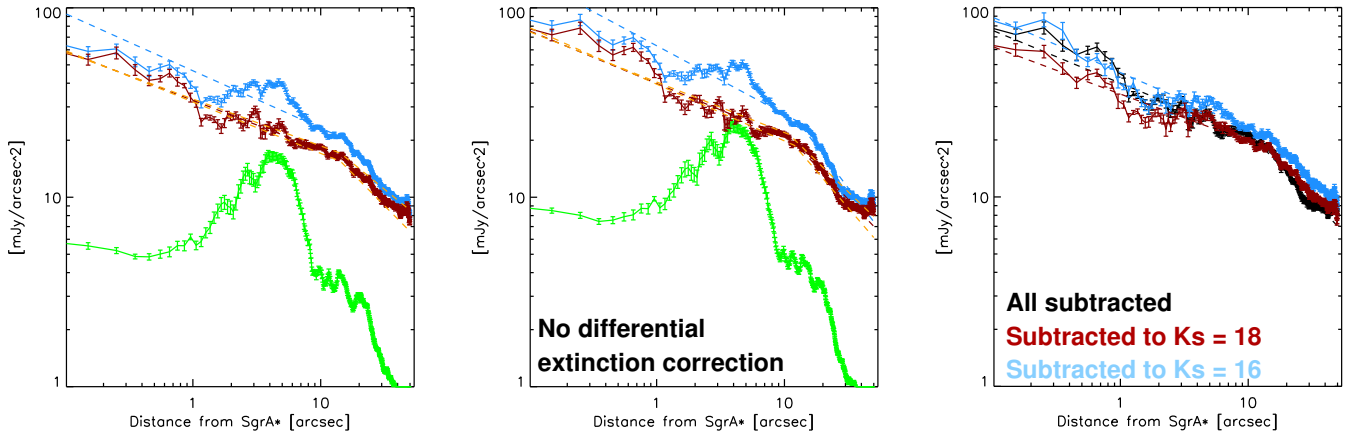


Fig. 5. Left: Mean diffuse SFB profiles in the K_S wide-field image before (blue) and after (red) subtraction of the scaled $\text{Pa } \alpha$ emission (green). The straight dashed lines are broken power-law fits to the data. The two orange dashed lines show the best broken power-law fits after subtracting or adding a standard deviation of the potential offset of the additive diffuse flux density. Middle: As left panel, but assuming a constant extinction for the entire field. Right: Corrected surface brightness for different brightness limits on subtracted stars. Subtraction of all detected stars in black, subtraction of $K_S < 16$ in blue, and subtraction of $K_S < 18$ in red.

star on the mean surface brightness at a given R will be negligible due to our use of the ROBUST_MEAN procedure, that rejects outliers and produces values very similar to the median. However, in small, crowded areas, such as the central arcseconds near Sgr A*, subtraction of faint stars may be significantly less complete so that, on average brighter stars remain in the image than in less crowded areas, which may create a systematic effect.

To examine this effect, in the right panel of Fig. 5 we plot the corrected K_S SFB profile for three cases. In each case, all the stars were subtracted to a different brightness limit: All detected stars, all stars $K_S < 18$, or all stars $K_S < 16$. The 3σ detection limit for stars in the K_S wide field image is about $K_S \approx 19$ (albeit at low completeness). As one can see, apart from an overall $\sim 10 - 20\%$ shift between the measured SFBs, the profiles look very similar. The best fit parameters - apart from the SFB normalisation, n_0 , - show only a small range of variation and agree within $1 - 2\sigma$ of their formal fit uncertainties: $R_0 = 0.54 - 0.56$ pc, $\Gamma_{in} = 0.25 - 0.29$, and $\Gamma_{out} = 0.62 - 0.66$.

3.2. Br γ

The surface brightness in the Br γ narrow band filter image is an interesting test case because here the emission from the ionised gas will provide a relatively large fraction of the overall diffuse emission. Again, we scaled the $\text{Pa } \alpha$ emission and subtracted it, after applying the extinction correction at the two bands. We fitted a simple power-law to the SFB at $R \lesssim 0.5$ pc. The resulting raw and corrected SFB profiles are shown in Fig. 6. The bump from the ionised gas at $1'' \lesssim R \lesssim 8''$ in the SFB profile disappears cleanly after subtraction of the scaled $\text{Pa } \alpha$ image. A simple power-law provides a very good fit, with the best-fit power-law exponent of $\Gamma_{in} = 0.25$. We do not fit any broken power-law because of the restricted FOV which will provide a poor constraint on the power-law at large R .

3.3. Deep K_S -band image

Here, we analyse the deep K_S broad band image that we use for measuring the stellar number surface density in Paper I. A simple power-law fit to the corrected SFB at $R \lesssim 0.5$ pc results in a power-law index of $\Gamma_{in} = 0.27$, see Fig. 7. The positive and

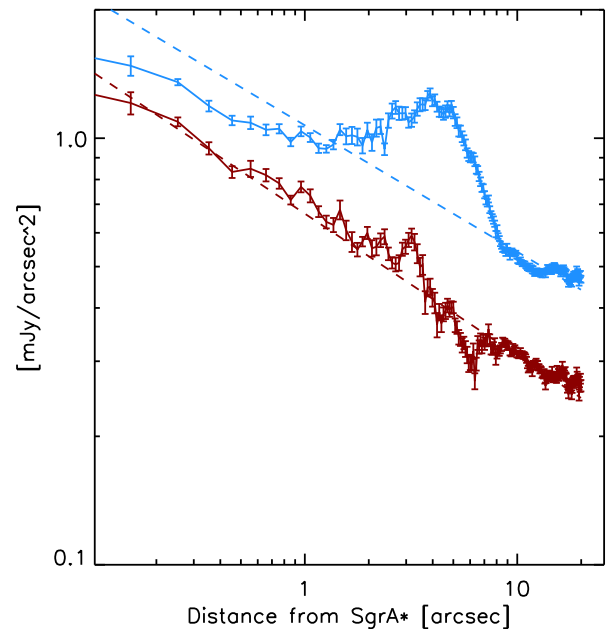


Fig. 6. Mean Brackett- γ diffuse SFB in annuli around Sgr A* before (blue) and after (red) subtraction of the scaled $\text{Pa } \alpha$ emission.

negative deviations of the corrected SFB from a power law at $R \approx 0.1$ pc is due to imperfect subtraction of the high concentration of very bright stars in this region. Most of the plots shown in this work show systematic effects in this region.

3.4. H-band image

Analysing the diffuse flux in an H band image represents, among others, a test in a regime, where differential extinction is stronger, where the sky background behaves in a different way, and where the ratio of line emission relative to $\text{Pa } \alpha$ is different. Hence, the H -band can be very helpful in constraining systematic effects. A simple power-law fit to the corrected SFB profile at $R \lesssim 0.5$ pc results in a power-law index of $\Gamma_{in} = 0.32$, see

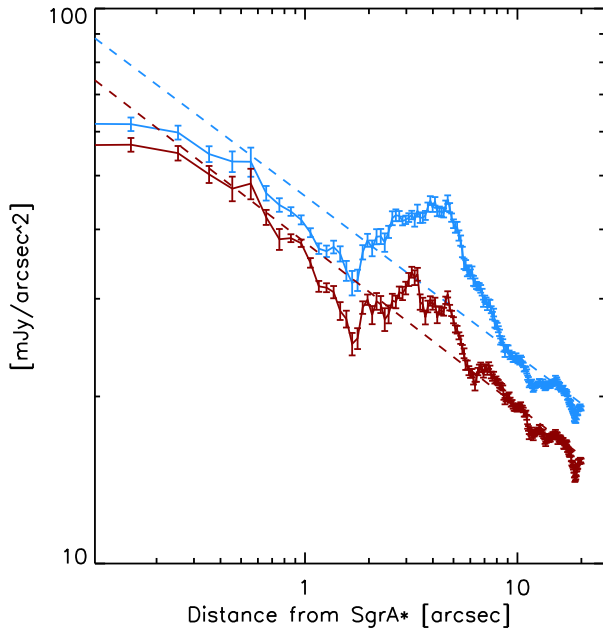


Fig. 7. Plot of K_S diffuse SFB in deep image (Paper I) before (blue) and after (red) subtraction of the scaled Pa- α emission.

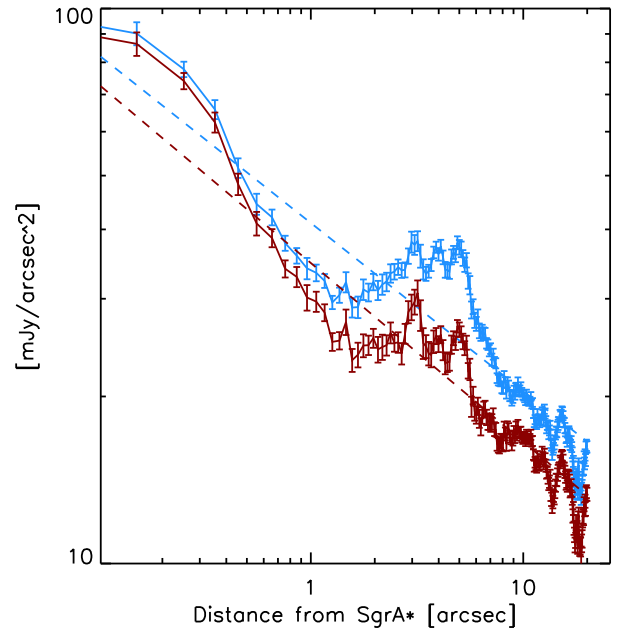


Fig. 8. Plot of H surface brightness in deep image (Paper I) before (blue) and after (red) subtraction of the scaled Pa- α emission.

Fig. 8. There appears to be an excess at projected radii $R < 0.5''$. This is the most crowded region, immediately around Sgr A*. Probably, the lower Strehl ratio at H may have led to a less complete source subtraction than at K_S . Since this excess is not consistently observed in all the filters examined here, we think that it is a spurious, systematic error. It does not alter our conclusions. Alternatively, instead of an excess at $R < 0.5$ we may be dealing with an over-subtraction of stellar flux due to our imperfect PSFs in the region $R \approx 1''$, which is dominated by the presence of bright stars (IRS 16NE, IRS 16C, IRS 16SW).

3.5. Deep K_S image with S13 camera

As a final test, we examine the diffuse light density in a deep, multi-epoch K_S -band image obtained with data from the S13 camera of NACO/VLT (see Paper I). Star subtraction through PSF fitting is particularly clean in this case and we did not have to mask the areas around bright stars IRS/16C, IRS 16NW, and IRS 16SW near Sgr A*. As Fig. 9 shows, a simple power law with an index of $\Gamma_{in} = 0.25$ provides a satisfactory fit to the radial dependency of the diffuse light density.

We tested again the systematics of subtracting the stars down to different limiting magnitudes ($K_{s,lim} = 16, 18, 20$). The power-law index changes between 0.25 and 0.29 and the plot looks similar in all cases as can be seen in the right panel of Fig. 9. We see a similar excess of diffuse flux at $R \lesssim 0.5''$ as in the the H -band profile. Compared to the NACO S27 K_S data there appears to be an offset of the SFB toward brighter values. We could not identify the source of this offset, but note that it does not affect our main conclusions, in particular the existence of a power-law cusp and its index.

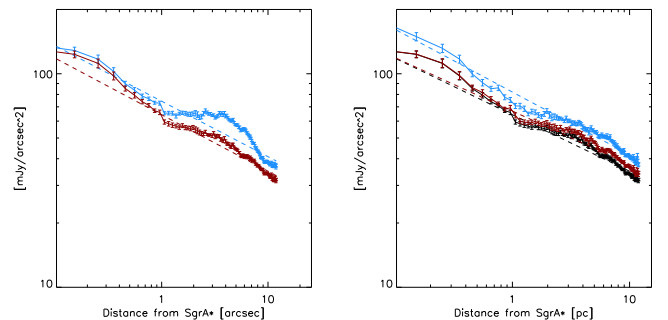


Fig. 9. Left: Plot of K_S surface brightness in deep image with S13 camera before (blue) and after (red) subtraction of the scaled Pa- α emission. Right: Corrected K_S surface brightness (equivalent to red points in left panel) when limiting the subtraction of stars to $K_S \leq 16$ (blue), $K_S \leq 18$ (red), and $K_S \leq 20$ (black).

Table 1. Best-fit power law indices for the diffuse stellar light inside of $R < 0.5$ pc.

Data	Γ_{in}
K_S , wide field	0.29
Br γ	0.25
K_S deep field	0.27
H	0.32
K_S S13	0.25

4. Discussion

4.1. Mean projected power-law index

As the preceding sections have shown, measuring the diffuse, stellar light around Sgr A* is a non-trivial undertaking and subject to potentially significant systematic effects. In particular, we have demonstrated that ionised gas contributes significantly to the measured diffuse flux at projected distances $R < 0.5$ pc from

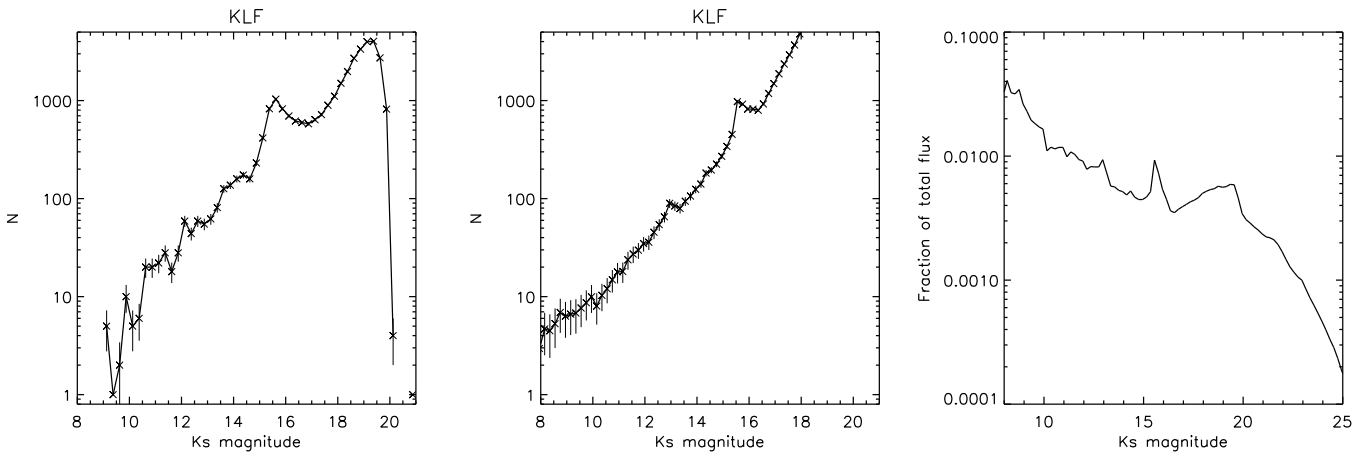


Fig. 11. Left: K_S luminosity function (KLF) measured on the deep K_S S13 NACO image. Middle: Simple model KLF for the case of continuous star formation, matched to the distance and mean extinction of the GC. Right: Flux density contributed by different types of stars, i.e. the KLF multiplied by the flux density of stars in a given bin.

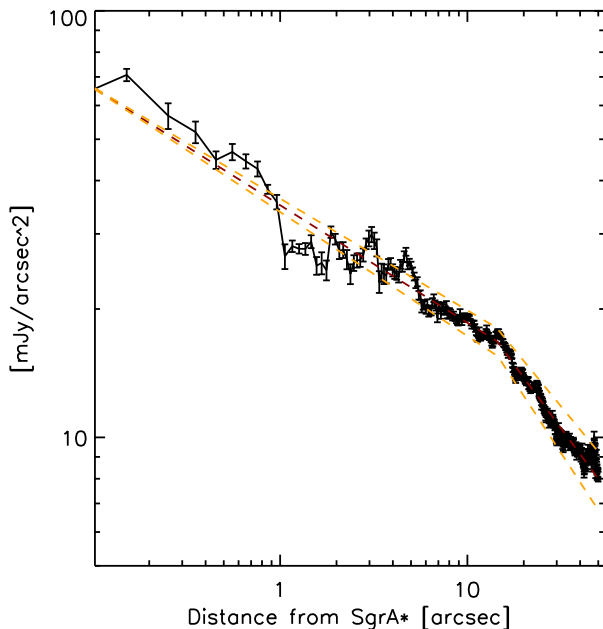


Fig. 10. MeanSFB profiles in the corrected and combined K_S S13 plus S27 wide-field image. The straight dashed lines are broken power-law fits to the data. The two orange dashed lines show the best broken power-law fits after subtracting or adding a standard deviation of the potential offset of the additive diffuse flux density.

Sgr A*, even when broad-band filters are used. This will result in an apparent steep increase of the diffuse flux at $R \lesssim 0.4$ pc and then an almost flat SFB profile in the innermost ~ 0.2 pc. The exact systematic error due to the ionised gas will depend, of course, on the filter used. It is very strong in Br γ (Fig. 6) and weaker in K_S (Fig. 7) and H (Fig. 8).

The subtraction of the flux of both the bright stars and the ionised gas is prone to systematic errors. Fortunately, these errors will change with the observing conditions, e.g., seeing and adaptive optics correction, camera used, or observing wavelength. For this reason, we have used several completely independent data sets that were obtained at different times and with significantly different setups: Deep and shallow images, broad

and narrow band observations, shorter and longer wavelength filters. It is satisfying to see that the resulting SFB profile is consistent among all the data sets.

All our different measurements of the projected stellar surface brightness can be fit well by the simple model of a single power-law at $R \lesssim 0.5$ pc. The corresponding power-law indices are consistent with each other and also with the power-law index inferred for the stellar number density of faint stars in this region, as determined in Paper I. Table 1 lists the resulting best-fit power-law indices for the projected diffuse light in the inner ~ 0.5 pc. From these independent measurements we obtain a best estimate of $\Gamma_{in} = 0.28 \pm 0.03$. This value agrees, within its uncertainties, with what we observe for the number density of the stars in the range $16.5 \lesssim K_S \lesssim 18.5$ that we present in Paper I. It also agrees with the value of $\Gamma = 0.34 \pm 0.04$ measured by Yusef-Zadeh et al. (2012) on NICMOS/HST images within $R \leq 5''/0.2$ pc. We conclude that the projected surface density distribution of stars around Sgr A* can be described well by a single power law with the same exponent for different stellar populations. The faint stars do not show a flat, core-like distribution as has been observed for the bright ($K_S \lesssim 15.5$) giants in the GC (Buchholz et al. 2009; Do et al. 2009; Bartko et al. 2010). *The faint stellar population around Sgr A* clearly displays a power-law cusp.* Given our measurements, assumptions, and analysis, we can exclude a flat projected core around Sgr A* with high confidence.

4.2. Optimised overall SFB profile

Mainly for illustrative purposes, we produced a "best" corrected image by combining the corrected S13 and S27 wide-field images. The images were matched via a least-squares minimisation of an additive offset and a multiplicative scaling factor. We then measured the SFB profile again as in section 3.1, that is we also estimated the uncertainty from inaccuracies in the sky background subtraction. A simple broken power-law provides a good fit to the data (see Fig. 10). The best-fit parameters are: $n_0 = 16.8 \pm 1.3$ mJy, $R_0 = 0.56 \pm 0.005$ pc, $\Gamma_{in} = 0.28 \pm 0.01$, and $\Gamma_{out} = 0.60 \pm 0.07$. We note that the broken power-law is a purely ad hoc choice, but does not necessarily represent the intrinsic structure of the cluster, which can be described well by a simple 3D power-law within a 3D distance $r < 3$ pc from Sgr A*, as we discuss in section 4.4

4.3. What kind of stars contribute to the diffuse SFB?

The stars that contribute dominantly to the diffuse light in our point-source subtracted images are fainter than $K_S = 18$. Figure 11 shows the K_S luminosity function (KLF) for the deep NACO S13 image. The turnover at $K_S \gtrsim 19$ is caused by incompleteness due to crowding and sensitivity. The peak around $K_S \approx 15.5$ arises from Red Clump (RC) stars. The middle panel shows a simple toy model KLF, based on continuous, constant star formation from $\log(t/\text{yr}) = 6.6$ to $\log(t/\text{yr}) = 10.13$ in steps of $\Delta(\log(t)) = 0.05$, with Solar metallicity, and assuming a Chabrier lognormal initial mass function (see, http://stev.oapd.inaf.it/cgi-bin/cmd_2.8 and Chabrier 2001; Bressan et al. 2012; Chen et al. 2014, 2015; Tang et al. 2014). We point out that we have not made any specific effort to match the model KLF to the measured one, except for applying a scaling factor. Studies of star formation history or metallicity are beyond the scope of this paper.

The right panel shows the fraction of the total flux contributed by the stars in the different bins of the model KLF. As can be seen, stars in the regime $K_S = 19 - 20$ do not differ significantly in their overall weight. Stars at $K_S \approx 21$, approximately solar mass MS stars, have a weight that is about 3 to 4 times lower. We thus expect stars with an apparent $K_S \approx 19 - 20$ at the GC to dominate our measurements of the diffuse light density. We expect these stars to be early G or late F type main sequence stars or sub-giant stars of similar mass. They will have masses $\lesssim 1.5 M_\odot$ and will live for several Gyrs (see also Fig. 16 in Schödel et al. 2007). They can thus be old enough to be dynamically relaxed and serve as tracers for the existence of a stellar cusp.

In Paper I we discuss and take into account the possible contamination of the surface number density of $K_S \approx 18$ stars by pre-main sequence (MS) stars from the most recent, a few Myr old star formation event in the central $R < 0.5$ pc (see, e.g., Genzel et al. 2010; Lu et al. 2013). Such contamination could, in principle, also be present in the diffuse light. While we cannot rule out this possibility with certainty, we point out that both the stellar number density profile and the profile of the diffuse stellar light probe different stellar masses and evolutionary stages. Also, the power-law index of the diffuse light density profile is consistent with the one derived for the surface number density counts of stars in the magnitude bins $16.5 \leq K_S \leq 17.5$ and $17.5 \leq K_S \leq 18.5$ (the latter after correction for pre-MS stars). Hence, while we cannot accurately constrain quantitatively the contamination of our tracer populations by stars that are too young to be dynamically relaxed, this contamination must either be small or very similar across the different stellar magnitude ranges. The similarity of the power-law indices that we find for different tracers suggests that they are indeed representative for the actual underlying structure of the old stars, which are expected to dominate the mass of the NSC (see, e.g., Pfuhl et al. 2011).

4.4. The 3D structure of the cluster

Our observations provide us with the surface brightness, but we would like to know the *intrinsic* structure of the NSC. This is not a trivial problem and requires a fairly complete and accurate knowledge of the stellar distribution on large scales both in and around the NSC. While we do not yet possess very detailed knowledge on the stellar population and its distribution, we can use the results of previous work on the large scale structure of the NSC combined with some basic or simplifying assumptions

(such as spherical symmetry) to provide an approximate, general picture.

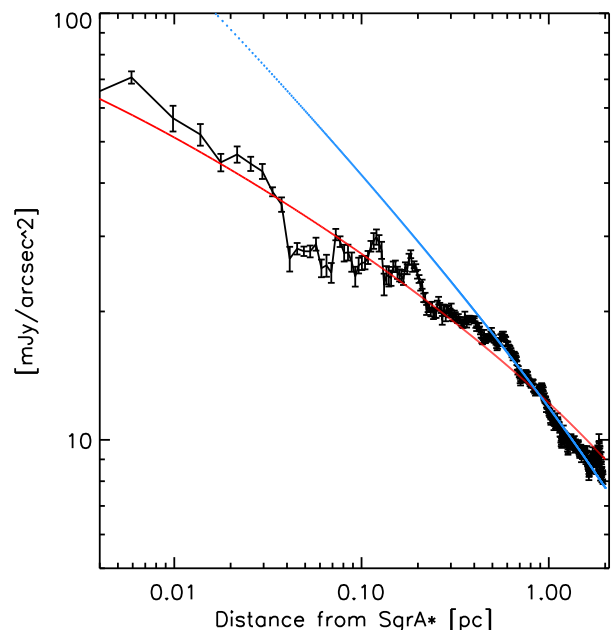


Fig. 12. SFB profile as shown in Fig. refFig:KsS13 with a best-fit 3D simple power-law overplotted as a solid red line. The blue line represents a forced fit with a power-law index of $\gamma = 1.5$, taking into account only data at $R > 0.4$ pc.

As a first, illustrative approximation to the problem, we can assume a simple power-law for the intrinsic 3D structure of the innermost parsecs of the cluster. It provides a surprisingly reasonable fit to the data, as shown by the red line in the left panel of Fig. 12. Since we need to project a three-dimensional structure onto two dimensions, the result of the fit depends on the boundaries, where we cut off the integration along the line of sight. The best-fit power-law index is $\gamma_{in} = 1.28$ for an outer integration boundary of 10 pc and $\gamma_{in} = 1.35$ for 20 pc. We note that, in projection, an intrinsic 3D power-law will not appear as a straight line on a double-logarithmic plot, but always flatten toward small radii. For this reason, broken power-laws can work well on the projected data (see Fig. 10). From theoretical work on the structure of a relaxed stellar cusp we would expect a power-law index of $\gamma_{in} \gtrsim 1.5$ for a low-mass tracer population. We have forced such a power-law fit to the data at $R > 0.3$ pc, as shown by the blue line in the plot. While it fits the data reasonably well at $R = 0.4 - 0.5$ pc, it is clearly too steep inside this range. We note that the distance $R = 0.4 - 0.5$ pc agrees with the projected size of the previously reported core or break radius of the cluster (see, e.g., Eckart et al. 1993; Schödel et al. 2007; Buchholz et al. 2009; Bartko et al. 2010).

Assuming an intrinsic simple power-law structure is, of course, an oversimplification because a large body of previous studies of the stellar density in the GC indicates that the nuclear cluster follows a density of approximately $n(r) \propto r^{-2}$ outside of the central parsec, with a steepening slope at larger distances (see, e.g., references and discussions in Launhardt et al. 2002; Schödel et al. 2007, 2014a; Fritz et al. 2016). A steepening density profile is also required to avoid that the cluster mass diverges. A caveat is that previous work was focussed on significantly brighter stars than what we are examining in the

present work. A study of the density of different stellar populations throughout the nuclear cluster out to distances beyond a few parsecs is beyond the scope of this work and will be addressed in a later paper. For simplicity – and because we assume that it is a good approximation on large scales – we will assume that the cluster shape is described well by the data in previous publications. Now we will explore the consequences of steeper density slope at larger distances on the inferred three-dimensional power-law near Sgr A*.

To constrain the stellar distribution on scales of approximately 1 to 10 pc, we use the data on the flux density of the NSC from Schödel et al. (2014a) and Fritz et al. (2016). The former used extinction-corrected Spitzer 4.5 μm surface brightness maps. The latter used extinction corrected near-infrared data from NACO/VLT, WFC/HST, and VISTA. Both data sets are not adequate to sample the light density profile inside $R \approx 1$ pc. The Spitzer data of Schödel et al. (2014a) are of low-angular resolution and long wavelength and completely dominated by a few bright stars and by emission from the mini-spiral in the inner parsec. The data from Fritz et al. (2016) are, in principle, more suitable, but are dominated by RC stars and brighter giants. As is well known and as we confirm in Paper I, these stars show a core-like structure within $R \leq 0.3$ pc from Sgr A*.

To isolate the nuclear cluster from the emission of the nuclear disk and Galactic Bulge, we subtracted a constant flux offset, which was taken as the mean of the flux in the range $15 \text{ pc} \leq R \leq 20 \text{ pc}$ (1 ± 0.1 and $6.4 \pm 0.35 \text{ mJy arcsec}^{-2}$ for the data sets of Schoedel et al. and Fritz et al., respectively). We scaled the data from Schödel et al. (2014a) and Fritz et al. (2016) to our data in the range $1.5 \text{ pc} \leq R \leq 2.0 \text{ pc}$. At $R < 1.5$ pc, we only use the data from our optimised SFB profile (see section 4.2). We then used a 3D *Nuker* model and projected it onto the sky to fit the measured surface brightness. We use the *Nuker* model (Lauer et al. 1995) in the form of “Equ. 1” of Fritz et al. (2016):

$$\rho(r) = \rho(r_b) 2^{(\beta-\gamma)/\alpha} \left(\frac{r}{r_b} \right)^{-\gamma} \left[1 + \left(\frac{r}{r_b} \right)^\alpha \right]^{(\gamma-\beta)/\alpha} \quad (2)$$

Here, r is the 3D distance from Sgr A*, r_b is the break radius, ρ is the 3D density, γ is the exponent of the inner and β the one of the outer power-law, and α defines the sharpness of the transition. The density was then projected along the line of sight via an integral:

$$\Sigma(R) = 2 \int_r^\infty \frac{r \rho(r) dr}{\sqrt{r^2 - R^2}} \quad (3)$$

For numerical reasons, to avoid a singularity, we could not integrate down to $r = R$ and therefore set the minimum $r = R + 0.001$ pc. The best-fit was found with the IDL MPFIT package (Markwardt 2009). Uncertainties were re-scaled to a reduced $\chi^2 = 1$. We fixed the parameter $\alpha = 10$ and used only data at $R \leq 20$ pc. The best fits, using the azimuthally averaged data of Schödel et al. (2014a) and Fritz et al. (2016), subtracted for a constant offset, are shown in Fig. 13.

There are a number of easily systematic uncertainties related to this procedure. Our primary test of robustness is, of course, the use of the completely independent data sets of Schödel et al. (2014a) and Fritz et al. (2016). We then explored the parameter space by repeating the fitting procedure for different cases:

- Fit with the azimuthally averaged data of Schödel et al. (2014a) as well as their profiles along the Galactic Plane and perpendicular to it, to examine the influence of the flattening of the nuclear cluster.

Table 2. Best-fit model parameters for the Nuker fits to the SFB profiles.

ID	r_b (pc)	γ	β	$\rho(r_b)$ (mJy pc $^{-3}$)
1 ^a	3.21 ± 0.15	1.15 ± 0.01	3.38 ± 0.17	0.67 ± 0.05
2 ^b	3.03 ± 0.20	1.17 ± 0.01	2.74 ± 0.12	0.72 ± 0.08
3 ^c	2.97 ± 0.21	1.18 ± 0.01	2.58 ± 0.10	0.73 ± 0.08
4 ^d	3.31 ± 0.15	1.14 ± 0.01	3.68 ± 0.22	0.65 ± 0.05
5 ^e	3.09 ± 0.15	1.15 ± 0.01	3.13 ± 0.14	0.72 ± 0.05
6 ^f	3.22 ± 0.15	1.15 ± 0.01	3.41 ± 0.18	0.67 ± 0.05
7 ^g	3.24 ± 0.20	1.16 ± 0.01	3.17 ± 0.15	0.65 ± 0.07
8 ^h	3.10 ± 0.19	1.16 ± 0.01	2.97 ± 0.12	0.70 ± 0.07
9 ⁱ	3.39 ± 0.22	1.16 ± 0.01	3.38 ± 0.18	0.61 ± 0.06
10 ^j	3.37 ± 0.16	1.18 ± 0.01	3.46 ± 0.19	0.66 ± 0.05
11 ^k	3.58 ± 0.24	1.21 ± 0.01	3.29 ± 0.17	0.57 ± 0.07

Notes. (a) Data from Schödel et al. (2014a), azimuthally averaged; 1 mJy arcsec $^{-2}$ constant emission subtracted.

(b) Data from Schödel et al. (2014a) perpendicular to Galactic Plane; 1 mJy arcsec $^{-2}$ constant emission subtracted.

(c) Data from Schödel et al. (2014a) along Galactic Plane; 1 mJy arcsec $^{-2}$ constant emission subtracted.

(d) Like (a), but 1.1 mJy arcsec $^{-2}$ constant emission subtracted.

(e) Like (a), but 0.9 mJy arcsec $^{-2}$ constant emission subtracted.

(f) Like (a), but using only data at $R \geq 0.05$ pc.

(g) Data from Fritz et al. (2016); 6.4 mJy arcsec $^{-2}$ constant emission subtracted.

(h) Like (g), but 6.05 mJy arcsec $^{-2}$ constant emission subtracted.

(i) Like (g), but 6.75 mJy arcsec $^{-2}$ constant emission subtracted.

(j) Like (a), with lower integration boundary at $r = R + 0.01$ pc.

(k) Like (g), with lower integration boundary at $r = R + 0.01$ pc.

- Constant flux offset: Fits with the mean of the flux in the range $15 \text{ pc} \leq R \leq 20 \text{ pc}$ subtracted as well as with the 1 sigma deviation of this flux added or subtracted.
- Fits with different settings for the minimum integration boundary ($r = 0.001, 0.005$, and 0.01 pc).
- Fits for different values of $\alpha = 10, 20, 40$.
- Fits to the entire data and fits limited to $R > 0.05$ pc to examine the influence of the innermost region around Sgr A*.

Table 2 summaries the best-fit parameters that we obtained for the model-fits to different data and under some different assumptions (We did not list all the tests that we ran on the data; the resulting parameters will range within the values listed in the table). The χ^2 values and the uncertainties of the different models and parameters are very similar to each other. We can obtain an approximate, mean model for the nuclear cluster by taking the mean of each best-fit parameter and its standard deviation (not error of the mean). We obtain $r_b = 3.2 \pm 0.2$ pc, $\gamma = 1.16 \pm 0.02$, $\beta = 3.2 \pm 0.3$, and $\rho(r_b) = 0.67 \pm 0.05 \text{ mJy pc}^{-3}$.

The break radius shows some degeneracy with the value of α , that we keep fixed in our fits. For very soft transitions between the outer and inner power laws, i.e. $\alpha < 10$, the break radius becomes larger, moving to values around 4 pc. Theory predicts that the cusp follows a power-law well inside the break radius and that the latter is on the order of the radius of influence of the black hole, which has been found to be ~ 3 pc (e.g., Alexander 2005; Feldmeier et al. 2014; Fritz et al. 2016), consistent with The Nuker law break radius determined here and in Paper I.

Here, we are most interested in the question of the existence of a stellar cusp. As we can see, γ can be determined very robustly and is > 0 . We can exclude a flat core with high confidence. An extensive analysis of the stellar number and flux surface density in the GC was presented in Fritz et al. (2016). They

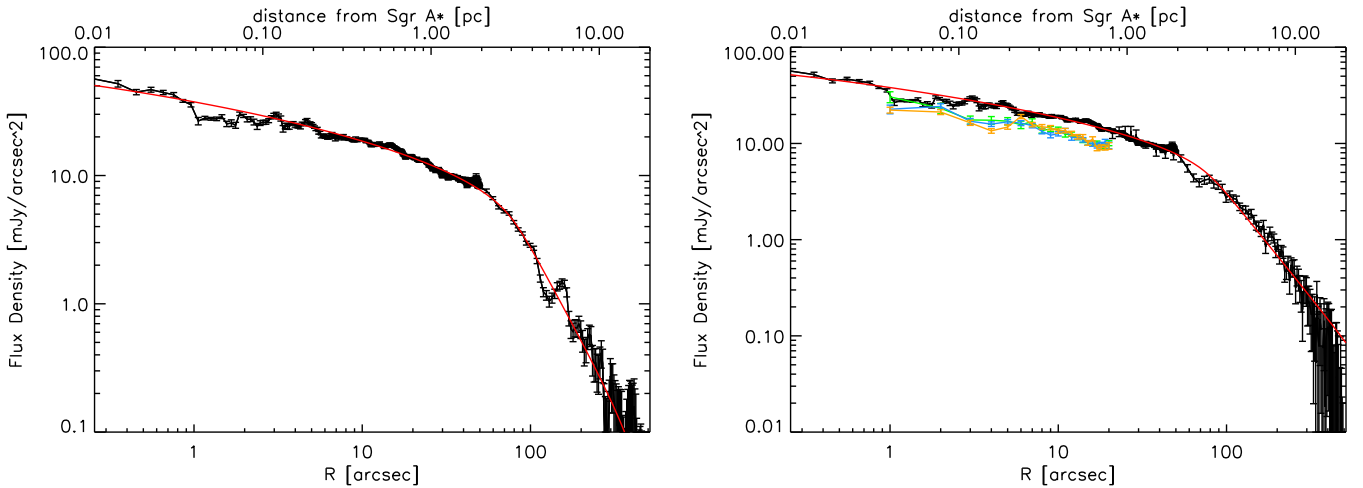


Fig. 13. Nuker model fits (red lines) to the diffuse SFB in the GC. Left: The data at $R \geq 1.5$ pc are the azimuthally averaged, extinction corrected Spitzer $4.5 \mu\text{m}$ data from Schödel et al. (2014a). Right: The data at $R \geq 1.5$ pc are the azimuthally averaged, extinction corrected near-infrared data from Fritz et al. (2016). The orange points and line show the stellar surface density data from Paper I for stars in the interval $K_S = 15 - 16$, blue for $K_S = 16.5 - 17.5$, and green for $K_S = 17.5 - 18.5$. For better visualisation, the stellar surface densities have been scaled by constant, arbitrary factors

fitted a so-called γ -model and found that the radial structure of the NSC in the innermost few 0.1 pc can be well described by a power-law with index $\gamma = 0.90 \pm 0.11$ for the stellar surface density and $\gamma = 0.76 \pm 0.08$ for the flux density. These values are flatter than what we have found here for the inner slope of the cluster. The main difference between their work and our work is that we focus on the diffuse emission of the faintest stellar population while their measurements are dominated by giant stars.

In Paper I we show that the stars of $K_S \approx 18$ show a projected surface density that is consistent with the one that we find here for the diffuse light, while the RC stars and brighter giants show a flattening inside a projected radius of $R \approx 0.3$ pc. In Fig. 13 we overplot the stellar surface number densities onto the plot of the surface brightness density of the diffuse light.

We find, however, larger values of γ in Paper I. For the $K_S \approx 18$ stars we find $\gamma = 1.29 \pm 0.03$. This discrepancy may indicate certain biases related to the different methods. For example, we may have underestimated the contamination by young stars in Paper I or over-estimated incompleteness due to crowding. Alternatively, we may have over-corrected the emission from ionised gas in this work or there may be a bias from the sky background subtraction resulting from an observational setup that was not optimised for measuring the unresolved, diffuse emission. There may also be other systematic effects at play that we have not considered. We note, however, that both values for γ exclude a flat, core-like profile with high confidence. We consider it reasonable to average the two values and adopt $\gamma = 1.23 \pm 0.06$ to describe the stellar cusp.

In Paper III we compare the measurements to N-body simulations and confirm the consistency between measurements and theory. The probably best explanation for the flatness of the observed cusp is mass segregation between stars of different masses in the inner parts of the nuclear cluster, which flattens the density profile of bright stars away from the $\gamma = 1.75$ prediction of Bahcall & Wolf (1976). In addition, due to repeated star formation and/or cluster infall not all the stars in the nuclear cluster may be old enough to be fully dynamically relaxed, which could cause a further modification of the central slope. Most models created so far assumed clusters with a single age stellar population that

evolved for many relaxation times. The NSC of the Milky Way, on the other hand, contains stellar population of different ages (see, e.g., Pfuhl et al. 2011). Also, the NSC may have had less than a Hubble time for two body relaxation processes to work, so it may not be fully relaxed. Paper III presents more elaborate theoretical models, based on direct N-body simulations, that provide results consistent with our data. We believe that the relative flatness of the cusp is the reason why it has eluded any clear confirmation for decades.

As concerns the value of β , which describes the density decrease at distances $r \gg r_b$, we find in Paper I a value $\beta_{\text{resolved}} = 2.1 \pm 0.1$, which agrees well with much earlier work on the large-scale structure of the NSC (see introduction and references in Schödel et al. 2007). In this work, however, we find a much steeper $\beta_{\text{unresolved}} = 3.2 \pm 0.3$. A value $\beta > 2$ is in agreement with the findings of Launhardt et al. (2002) and is also required if the NSC mass is to converge for large radii. Again, an intermediate value with a larger uncertainty may be closer to reality. In any case, we note that it is beyond the scope of this paper to determine an accurate value for β . Its precise value does not affect the main conclusions of this work. As a final note, the data used here to constrain the cluster structure at large R reflect a much brighter tracer population than the stars that dominate the diffuse emission from unresolved stars in our NACO images.

4.5. Density of stars near Sgr A*, enclosed stellar mass

For observational purposes, it is of great interest to obtain a rough estimate of the surface number density of unresolved stars at $R = 0.25''$ ($R = 0.01$ pc). On the one hand, the results from Paper I show that the surface number density of stars at $17.5 \leq K_S \leq 18.5$ is about 20 arcsec^{-2} at $R = 0.25''$. Applying this normalisation to the model KLF from section 4.3, we obtain $64 \text{ stars arcsec}^{-2}$ in the interval $18.5 \leq K_S \leq 19.5$ and $105 \text{ stars arcsec}^{-2}$ in the interval $19.5 \leq K_S \leq 20.5$. If we use the surface flux density derived in this work, on the other hand, we obtain somewhat higher values. The extinction-corrected surface flux density estimated at $R = 0.01$ pc is about $50 \text{ mJy arcsec}^{-2}$, which results, for the same model KLF, in ~ 1.7 times higher densities

Table 3. Stellar mass densities near Sgr A* and total stellar mass within $r = 1$ pc.

ID	$\rho(1 \text{ pc})$ ($M_{\odot} \text{ pc}^{-3}$)	$\rho(0.1 \text{ pc})$ ($M_{\odot} \text{ pc}^{-3}$)	$\rho(0.01 \text{ pc})$ ($M_{\odot} \text{ pc}^{-3}$)	$m_{\text{stellar}}(1 \text{ pc})$ M_{\odot}
1 ^a	1.1×10^5	$\rho = 1.7 \times 10^6$	$\rho = 2.4 \times 10^7$	0.8×10^6
2 ^b	1.7×10^5	$\rho = 2.4 \times 10^6$	$\rho = 3.5 \times 10^7$	1.1×10^6
3 ^c	0.8×10^5	$\rho = 1.2 \times 10^6$	$\rho = 1.7 \times 10^7$	0.5×10^6
4 ^d	1.6×10^5	$\rho = 2.3 \times 10^6$	$\rho = 3.4 \times 10^7$	1.1×10^6
5 ^e	1.2×10^5	$\rho = 1.7 \times 10^6$	$\rho = 2.5 \times 10^7$	0.8×10^6

Notes. ^(a) Normalisation to a total cluster mass of $2.5 \times 10^7 M_{\odot}$ (Schödel et al. 2014a).

^(b) Normalisation to a mass of $1.4 \times 10^7 M_{\odot}$ within 4.2 pc of Sgr A* (Feldmeier et al. 2014).

^(c) Normalisation to a mass of $6.09 \times 10^6 M_{\odot}$ within 3.9 pc of Sgr A* (Fritz et al. 2016).

^(d) Normalisation to a mass of $1.1 \times 10^6 M_{\odot}$ within 1 pc of Sgr A* (Schödel et al. 2009).

^(e) Normalisation to a mass of $8.94 \times 10^6 M_{\odot}$ within 3.9 pc of Sgr A* (Chatzopoulos et al. 2015).

of 107 stars arcsec^{-2} in the interval $18.5 \leq K_s \leq 19.5$ and 175 stars arcsec^{-2} in the interval $19.5 \leq K_s \leq 20.5$. This discrepancy is smaller than a factor of 2 and can be explained by various systematic uncertainties, such as the assumed luminosity function. NIR cameras at the next generation of extremely large telescopes, such as MICADO/E-ELT (Davies & Genzel 2010), will have angular resolutions of $\lesssim 10$ mas FWHM, and thus be able to resolve surface number densities on the order of 1000 stars arcsec^{-2} (the actual performance will depend on the dynamical range and luminosity function of the observed field). Hence, the future generation of ground-based, AO-assisted telescopes will be able to observe the stellar cusp around Sgr A* directly, down to about one solar mass stars. The high stellar surface density is encouraging for interferometric observations of the immediate environment of Sgr A* with an instrument such as GRAVITY/VLTI (Eisenhauer et al. 2011), if it can reach the required high sensitivity.

Another value of interest is the mass density near Sgr A* and the total enclosed mass within 1 pc of Sgr A*. Using our best-fit Nuker-law parameters, we have computed the mass density at distances of $r = 1, 0.1$, and 0.01 pc from Sgr A*, using five different normalisations of the enclosed mass, four of them dynamical (Schödel et al. 2009; Feldmeier et al. 2014; Chatzopoulos et al. 2015; Fritz et al. 2016) and one of them based on mass-to-light ratio (Schödel et al. 2014a). The values are listed in Tab. 3 and agree within factors of $\lesssim 2$.

Densities in excess of a few $10^7 M_{\odot} \text{ pc}^{-3}$ are reached at $r < 0.01$ pc of Sgr A*, which corresponds roughly to the apo-centre of the orbit of the short-period star S2/S0-2 (e.g., Boehle et al. 2016). This is comparable to what has been inferred by some models for the central density of Omega Centauri (Noyola et al. 2008). We note that 0.01 pc correspond to about $0.25''$ or a few resolution elements of a 10m-class telescope in the NIR at the distance of the GC. In spite of this high density, the small volume implies that this corresponds to only $180 \pm 20 M_{\odot}$ (taking the mean over the different mass normalisations).

From the different values given in Table 3, we estimate a total stellar mass within $r = 0.1$ pc of Sgr A* of about $1.3 \pm 0.2 \times 10^4 M_{\odot}$, smaller than, but of the same order of magnitude as, the value given by Yusef-Zadeh et al. (2012). The total mass within $r = 1$ pc of Sgr A* is $9.0 \pm 0.1 \times 10^5 M_{\odot}$. Depending on the

normalisation, the stellar mass within a spherical volume of $r = 2 - 3$ pc is equal to the mass of Sgr A*. As a note of caution, we remind the reader here that the Nuker model assumed here for the NSC does not take into account the mass from the nuclear bulge or other stellar components that do not form part of the NSC, but may overlap with it. Therefore, our model should not be used to compute the mass enclosed at large r .

We point out that here we assume a constant mass-to-light ratio throughout the NSC. This may result in an under-estimation of the enclosed mass of the NSC at small radii. Theoretical considerations and simulations predict an accumulation of stellar-mass black holes in an invisible, steep ($\gamma \approx -1.75$) cusp around Sgr A* (e.g., Morris 1993; Merritt 2006; Alexander & Hopman 2009; Preto & Amaro-Seoane 2010). This cusp is actually steeper when one considers realistic number fractions for the stellar population, which leads to a more efficient segregation of the masses. In particular, Alexander & Hopman (2009), Preto & Amaro-Seoane (2010), and Amaro-Seoane & Preto (2011) find in their models that the cusp for their “heavy” stars, the precursors of stellar-mass black holes, build up a cusp with $\gamma \approx -2$. They refer to this finding as “strong mass segregation”. Depending on the properties of this putative black hole cusp, the enclosed mass at small distances from Sgr A* may be significantly higher than the estimates provided here. The most recent constraint on the extended mass within 0.01 pc of Sgr A* from the orbital analysis of individual stars is that it must be less than $1.3 \times 10^5 M_{\odot}$ (Boehle et al. 2016). Hence, the mass density estimated here can be easily accommodated by current dynamical analyses.

5. Conclusions

This paper presents the radial surface brightness profile of the diffuse emission in high angular resolution, point source-subtracted images of the GC. After taking into account the contamination of the diffuse light by line emission from ionised gas, we argue that the diffuse emission arises from a faint, unresolved stellar population with magnitudes of $K_s = 19 - 20$. This corresponds to main sequence stars or sub-giant stars with masses of $\lesssim 1.5 M_{\odot}$. These stars can plausibly live long enough on the main sequence to be dynamically relaxed and thus to serve as a tracer population for a stellar cusp around the central black hole of the Milky Way.

We find that the projected surface brightness profile can be fitted well by a power-law slope with an index of $\Gamma_{in} = 0.28 \pm 0.03$ at $R < 0.5$ pc. This value is somewhat smaller, but consistent with what we find for the stellar surface number density of $K_s \approx 18$ (observed magnitude) stars in Paper I. The fact that the work in this paper and in Paper I use different methodologies gives us great confidence in our results.

Translating these results into an intrinsic, three-dimensional description of the cluster is not trivial, but by using previous studies of the cluster morphology on large scales as constraints, along with a spherical approximation, we find that the cluster can be described well by a Nuker law within about 20 pc of the central black hole. The break radius is 3.2 ± 0.2 pc, similar to the radius of influence of Sgr A*, which is estimated in this work to be of that order, and coincides with theoretical estimates (e.g., Alexander 2005). The three-dimensional density inside of the break radius follows a power law with an exponent $\gamma_{in} = 1.16 \pm 0.02$. A core-like distribution of the faint stars can thus be firmly excluded. From a comparison between the results for the faint, unresolved stellar population and the $K_s \approx 18$ re-

solved population (Paper I), we argue that a robust estimate for the power-law index of the cusp is $\gamma = 1.23 \pm 0.05$.

An underlying assumption of our work is that the faint emission arises indeed mostly from stars old enough to be dynamically relaxed. A possible source of concern could be contamination by pre-main sequence stars in the region of the few million year-old starburst within $R = 0.5$ pc of Sgr A*. However, we deem this unlikely because we find consistently the same power-law, for the diffuse light as well as for resolved stars in the magnitude range of $K_S = 16 - 18$ (see Paper I).

The stellar cusp identified in this work and in Paper I is significantly flatter than the one predicted for single-mass stars around a massive central black hole $\gamma_{\text{theor}} = 1.75$, or for low-mass stars in a cluster composed of two mass groups ($\gamma_{\text{theor}} = 1.5$). In contrast to the simplifying assumptions of previous theoretical work, the nuclear cluster at the GC has undergone multiple epochs of star formation and/or cluster infall. Thus, not all the stars may be old enough to be fully dynamically relaxed. As we will elaborate in Paper III, our observations nicely agree with the detailed, direct-summation Nbody simulations. In Paper III we compare the measurements to N-body simulations and confirm the consistency between measurements and theory.

The flatness of the cusp is one of the main reasons why it has eluded detection so far. The second reason is that the giant stars brighter than $K_S \approx 16$ dominated all previous attempts at determining the NSC's structure. However, these stars show a core-like profile within $R \approx 0.3$ pc (see Paper I and discussion and references therein).

We summarise our conclusions here:

1. Observations confirm the existence of a simple power-law cusp around Sgr A*, with a power-law index $\gamma = 1.23 \pm 0.05$.
2. The cusp is shallower than what is predicted by theory.
3. The existence of a cusp in our Galaxy supports the existence of stellar cusps in other, similar systems that are composed of a nuclear cluster and a massive black hole.
4. The existence of stellar cusps is an important prerequisite for the observation of EMRIs with gravitational wave detectors.
5. The bright giants and the Red Clump stars at the GC do not show the same distribution as the fainter stars. Either the bright giants are, on average, younger than the fainter stars and are not yet dynamically sufficiently well relaxed, or some mechanism has altered the appearance of this population: Very likely, the envelope of giants were removed by colliding with the fragmenting gas disc at the GC which later turned into the observed stellar disc of young, massive stars (Amaro-Seoane & Chen 2014).

Future research needs to be done to refine our understanding of the cusp at the GC. On the observational side, we need to infer robust data on the large-scale two-dimensional distribution of stars out to about 10 pc from Sgr A* with high sensitivity and angular resolution. We will then be able to reconstruct the intrinsic three-dimensional profile of the cluster. The next step will then be an accurate determination of the different types of faint stars near Sgr A* (e.g.: Which ones are pre-MS stars?) in order to understand the age structure of the nuclear star cluster. At least some of this future work can only be done with a 30m-class telescope. Observations with the next generation of telescopes can test the predictions on stellar number densities from our work.

Acknowledgements. The research leading to these results has received funding from the European Research Council under the European Union's Seventh Framework Programme (FP7/2007-2013) / ERC grant agreement n° [614922]. PAS acknowledges support from the Ramón y Cajal Programme of the Ministry of Education and Science of Spain. This work is based on observations made

with ESO Telescopes at the La Silla Paranal Observatory under programmes IDs 083.B-0390, 183.B-0100 and 089.B-0162. We thank the staff of ESO for their great efforts and helpfulness.

References

- Alexander, T. 1999, *ApJ*, 527, 835
 Alexander, T. 2005, *Phys. Rep.*, 419, 65
 Alexander, T. & Hopman, C. 2009, *ApJ*, 697, 1861
 Amaro-Seoane, P. 2012, *ArXiv e-prints* [arXiv:1205.5240]
 Amaro-Seoane, P., Aoudia, S., Babak, S., et al. 2013, *GW Notes*, Vol. 6, p. 4-110, 6, 4
 Amaro-Seoane, P., Aoudia, S., Babak, S., et al. 2012, *Classical and Quantum Gravity*, 29, 124016
 Amaro-Seoane, P. & Chen, X. 2014, *ApJ*, 781, L18
 Amaro-Seoane, P., Freitag, M., & Spurzem, R. 2004, *MNRAS*, 352, 655
 Amaro-Seoane, P., Gair, J. R., Freitag, M., et al. 2007, *Classical and Quantum Gravity*, 24, 113
 Amaro-Seoane, P. & Preto, M. 2011, *Classical and Quantum Gravity*, 28, 094017
 Bahcall, J. N. & Wolf, R. A. 1976, *ApJ*, 209, 214
 Bartko, H., Martins, F., Trippe, S., et al. 2010, *ApJ*, 708, 834
 Boehle, A., Ghez, A. M., Schödel, R., et al. 2016, *ApJ*, 830, 17
 Bressan, A., Marigo, P., Girardi, L., et al. 2012, *MNRAS*, 427, 127
 Buchholz, R. M., Schödel, R., & Eckart, A. 2009, *A&A*, 499, 483
 Chabrier, G. 2001, *ApJ*, 554, 1274
 Chatzopoulos, S., Fritz, T. K., Gerhard, O., et al. 2015, *MNRAS*, 447, 948
 Chen, Y., Bressan, A., Girardi, L., et al. 2015, *MNRAS*, 452, 1068
 Chen, Y., Girardi, L., Bressan, A., et al. 2014, *MNRAS*, 444, 2525
 Christopher, M. H., Scoville, N. Z., Stolovy, S. R., & Yun, M. S. 2005, *ApJ*, 622, 346
 Dale, J. E., Davies, M. B., Church, R. P., & Freitag, M. 2009, *MNRAS*, 393, 1016
 Davies, R. & Genzel, R. 2010, *The Messenger*, 140, 32
 Do, T., Ghez, A. M., Morris, M. R., et al. 2009, *ApJ*, 703, 1323
 Dong, H., Wang, Q. D., Cotera, A., et al. 2011, *MNRAS*, 417, 114
 Dong, H., Wang, Q. D., & Morris, M. R. 2012, *MNRAS*, 425, 884
 Eckart, A., Genzel, R., Hofmann, R., Sams, B. J., & Tacconi-Garman, L. E. 1993, *ApJ*, 407, L77
 Eisenhauer, F., Perrin, G., Brandner, W., et al. 2011, *The Messenger*, 143, 16
 Ekers, R. D., van Gorkom, J. H., Schwarz, U. J., & Goss, W. M. 1983, *A&A*, 122, 143
 Feldmeier, A., Neumayer, N., Seth, A., et al. 2014, *A&A*, 570, A2
 Frank, J. & Rees, M. J. 1976, *MNRAS*, 176, 633
 Fritz, T. K., Chatzopoulos, S., Gerhard, O., et al. 2016, *ApJ*, 821, 44
 Genzel, R., Eisenhauer, F., & Gillessen, S. 2010, *Reviews of Modern Physics*, 82, 3121
 Genzel, R., Schödel, R., Ott, T., et al. 2003, *ApJ*, 594, 812
 Gong, X., Lau, Y.-K., Xu, S., et al. 2015, in *Journal of Physics Conference Series*, Vol. 610, *Journal of Physics Conference Series*, 012011
 Gurevich, A. V. 1964, *Geomagnetism and Aeronomy*, 4, 192
 Hopman, C. & Alexander, T. 2005, *ApJ*, 629, 362
 Kieffer, T. F. & Bogdanović, T. 2016, *ApJ*, 823, 155
 Lauer, T. R., Ajhar, E. A., Byun, Y.-I., et al. 1995, *AJ*, 110, 2622
 Launhardt, R., Zylka, R., & Mezger, P. G. 2002, *A&A*, 384, 112
 Lightman, A. P. & Shapiro, S. L. 1977, *ApJ*, 211, 244
 Lo, K. Y. & Claussen, M. J. 1983, *Nature*, 306, 647
 Lu, J. R., Do, T., Ghez, A. M., et al. 2013, *ApJ*, 764, 155
 Lu, J. R., Ghez, A. M., Hornstein, S. D., Morris, M., & Becklin, E. E. 2005, *ApJ*, 625, L51
 Lu, J. R., Ghez, A. M., Hornstein, S. D., et al. 2009, *ApJ*, 690, 1463
 Markwardt, C. B. 2009, in *Astronomical Society of the Pacific Conference Series*, Vol. 411, *Astronomical Data Analysis Software and Systems XVIII*, ed. D. A. Bohlender, D. Durand, & P. Dowler, 251
 Merritt, D. 2006, *Reports on Progress in Physics*, 69, 2513
 Morris, M. 1993, *ApJ*, 408, 496
 Nishiyama, S., Tamura, M., Hatano, H., et al. 2009, *ApJ*, 696, 1407
 Noyola, E., Gebhardt, K., & Bergmann, M. 2008, *ApJ*, 676, 1008
 Paumard, T., Genzel, R., Martins, F., et al. 2006, *ApJ*, 643, 1011
 Peebles, P. J. E. 1972, *ApJ*, 178, 371
 Pfuhl, O., Fritz, T. K., Zilka, M., et al. 2011, *ApJ*, 741, 108
 Preto, M. & Amaro-Seoane, P. 2010, *ApJ*, 708, L42
 Schödel, R. 2010, *A&A*, 509, A260000+
 Schödel, R., Eckart, A., Alexander, T., et al. 2007, *A&A*, 469, 125
 Schödel, R., Feldmeier, A., Kunneriath, D., et al. 2014a, *A&A*, 566, A47
 Schödel, R., Feldmeier, A., Neumayer, N., Meyer, L., & Yelda, S. 2014b, *Classical and Quantum Gravity*, 31, 244007
 Schödel, R., Merritt, D., & Eckart, A. 2009, *A&A*, 502, 91
 Schödel, R., Najarro, F., Muzic, K., & Eckart, A. 2010, *A&A*, 511, A18+
 Tang, J., Bressan, A., Rosenfield, P., et al. 2014, *MNRAS*, 445, 4287
 Wang, Q. D., Dong, H., Cotera, A., et al. 2010, *MNRAS*, 402, 895
 Yusef-Zadeh, F., Bushouse, H., & Wardle, M. 2012, *ApJ*, 744, 24